In-cloud formation of secondary species in iron-containing particles

Qinhao Lin[1], Xinhui Bi[1,*], Guohua Zhang[1], Yuxiang Yang[1,2], Long Peng[1,2], Xiufeng Lian[1,2], Yuzhen Fu[1,2], Mei Li[3], Duohong Chen[4], Mark Miller[5], Ji Ou[6], Mingjin Tang[1], Xinming Wang[1], Ping'an Peng[1], Guoying Sheng[1], and Zhen Zhou[3]

[1] State Key Laboratory of Organic Geochemistry and Guangdong Key Laboratory of Environmental Resources Utilization and Protection, Guangzhou Institute of Geochemistry, Chinese Academy of Sciences, Guangzhou 510640, PR China

[2] University of Chinese Academy of Sciences, Beijing 100039, PR China

[3] Institute of Mass Spectrometer and Atmospheric Environment, Jinan University, Guangzhou 510632, PR China

[4] State Environmental Protection Key Laboratory of Regional Air Quality Monitoring, Guangdong Environmental Monitoring Center, Guangzhou 510308, PR China

[5] Department of Environmental Sciences, Rutgers, the State University of New Jersey, New Brunswick, NJ 08901, USA

[6] Shaoguan Environmental Monitoring Center, Shaoguan 512026, PR China

*Correspondence to: Xinhui Bi (bixh@gig.ac.cn)

Abstract. The increase of secondary species through cloud processing potentially increases aerosol iron (Fe) bioavailability. In this study, a ground-based counterflow virtual impactor coupled with a real-time single-particle aerosol mass spectrometer was used to characterize the formation of secondary species in Fe-containing cloud residues (dried cloud droplets) at a mountain site in southern China for nearly one month during the autumn of 2016. Fe-rich, Fe-dust, Fe-elemental carbon (Fe-EC), and Fe-vanadium (Fe-V) cloud residual types were obtained in this study. The Fe-rich particles, related to combustion sources, contributed 84% (by number) to the Fe-containing cloud residues, and the Fe-dust particles represented 12%. The remaining 4% consisted of the Fe-EC and Fe-V particles. It was found that above 90% (by number) of Fe-containing particles had already contained sulfate before cloud events, leading to no distinct change in number fraction (NF) of sulfate during cloud events. Cloud processing contributed to the enhanced NFs of nitrate, chloride, and oxalate in the Fe-containing cloud residues. However, the in-cloud formation of nitrate and chloride in the Fe-rich type was less obvious relative to the Fe-dust type. The increased NF of oxalate in the Fe-rich cloud residues was produced via aqueous oxidation of oxalate precursors (e.g., glyoxylate). Moreover, Fe-driven Fenton reaction likely increase the formation rate of aqueous-phase OH, improving the conversion of the precursors to oxalate in the Fe-rich cloud residues. During daytime, the decreased NF of oxalate in the Fe-rich cloud residues was supposed to be due to the photolysis of Fe-oxalate complexes. This work emphasizes the role of combustion Fe sources in participating in cloud processing and has important implications for evaluating Fe bioavailability from combustion sources during cloud processing.

Keywords: Fe-containing particles, oxalate, cloud residues, secondary species, cloud

46   processing, southern China

1 Introduction

Iron (Fe)-containing particles were frequently detected in the atmosphere, with concentration ranging from 10 ng/m^3 over remote marine environment to 28 μg/m^3 near desert areas (Zhang et al., 2003; Fomba et al., 2013). The Fe-containing particles have an adverse effect on human health, causing issues such as DNA strand breakage and cell damage (See et al., 2007; Abbaspour et al., 2014). Some researchers also reported that Fe solubility might be an important criterion for toxicity in lung fluid (Costa and Dreher, 1997). Bioavailable Fe derived from atmospheric aerosol deposition can limit the photosynthetic activity of marine phytoplankton in high-nutrient low-chlorophyll waters, indirectly affects oceanic carbon uptake and storage, and has feedback effects on climate (Jickells et al., 2005). The Fe-containing particles can contain various species, such as calcium (Ca), silicon (Si), aluminum (Al), vanadium (V), elemental carbon (EC), secondary inorganic and organic species (Zhang et al., 2014; Bi et al., 2016; Dall'Osto et al., 2016). The presence and coexistence of various species could further modify the effects of the Fe-containing particles on human health, ecology, and climate (Mahowald et al., 2005; Abbaspour et al., 2014).

The Fe-containing particle sources mainly include mineral dust and combustion emissions (e.g., biomass burning, coal combustion, and iron/steel industrial activities) (Jickells et al., 2005; Sedwick et al., 2007). Abundant Ca, Si, and Al often exist in the Fe-containing particles from mineral dust sources (Sullivan et al. 2007a), while the Fe-containing particles from combustion sources usually contains EC and other metals, as well as minor amounts of Ca (Li et al., 2013; Dall'Osto et al., 2016). The chemical properties of the Fe-containing particles depend on its emission sources and could also be modified by the formation of secondary species during

69   atmospheric processes (Zhang et al., 2014; Dall'Osto et al., 2016; Lin et al., 2017). The Fe-

70   containing particles in East Asian outflows was often observed to be internally mixed with

71   sulfate, mostly due to the large amount of SO_2 from coal in China (Furutani et al., 2011; Moffet

72   et al., 2012; Li et al., 2013). Sullivan et al. (2007a) proposed that the enrichment of sulfate in

73   the Asian mineral dust was possibly due to the Fe-catalyzed oxidation of SO_2 to sulfate. In

74   European urban areas, Dall'Osto et al. (2016) found that the Fe-containing particles was

75   internally mixed with nitrate rather than sulfate, and was most likely associated with urban

76   traffic activities. The frequent measurement of oxalate in the Fe-containing particles was

77   produced via photochemical and/or aqueous oxidation over East Asia (Sullivan and Prather

78   2007; Yang et al, 2009; Cheng et al, 2017).

79   The above observations about atmospheric processes of the Fe-containing particles were

80   mainly performed in environments with low aerosol liquid water content. Cloud processing

81   accompanied by high amounts of water played a vital role in the formation of secondary species

82   (e.g., sulfate, nitrate, chloride, ammonium, and oxalate) through the partitioning of gas-into-

83   aqueous phases or heterogeneous/multiphase processes (Sellegri et al. 2003; Lim et al., 2010;

84   Chang et al., 2011; Harris et al., 2013). For example, one model study had estimated that up to

85   80% of the total production of sulfate globally originated from aqueous reactions (Tsai et al.,

86   2010). The presence of Fe in cloud droplets also allowed the conversion of SO_2 to sulfate via

87   Fe-catalyzed autoxidation reactions (Harris et al., 2013). Furthermore, Fe chemistry involved

88   in Fenton or Fenton-like reactions in cloud droplets yielded OH-radicals that can induce the

89   conversion of glyoxylic acid to low volatility organic aerosols (e.g., oxalate) (Ervens et al.,

90   2011). Various Fe-containing particle sources (such as dust and anthropogenic sources) might

91   have different effects on the in-cloud formation of secondary species due to their different

92   physicochemical properties (e.g., alkalinity) of these sources (Deguillaume et al., 2005).

93   However, research on the effects of cloud processing on the formation of secondary species in

94   various Fe-containing particle types remains poorly understood.

95   We have previously used a ground-based counterflow virtual impactor (GCVI) combined and

96   a real-time single-particle aerosol mass spectrometer (SPAMS) to characterize chemical

97   composition or mixing state of cloud residues (Lin et al., 2017), mixing state and cloud

98   scavenging of the EC-containing particles (Zhang et al., 2017a), and the in-cloud formation of

99   oxalate (Zhang et al., 2017b) at a mountain site, southern China. In this study, the same

100 combined technology was utilized to obtain information on the characteristics and potential

101 sources of Fe-containing cloud residues. Additionally, Fe-containing interstitial (nonactivated

102 particles) and cloud-free particles were also analyzed. The impact of cloud processing on the

103 formation of sulfate, nitrate, chloride, ammonium, oxalate precursors, and oxalate in various

104 Fe-containing particle types were addressed.

105

106 **2 Experimental section**

107 **2.1 Sampling site**

108 The sampling site was situated in the Nanling Background Station (112°53'56'' E, 24°41'56''

109 N, 1690 m a.s.l.) in southern China. The sampling site was in an acid precipitation region

110 (Annual Environment Report of China in 2016, http://www.mep.gov.cn/hjzl/). Due to the site

111 being surrounded by a national park forest (273 km^2), it was minimally affected by local

112 anthropogenic activities. However, it might be subjected to polluted air masses from the

southern Pearl River Delta city groups or from northern China (Lin et al. 2017). A detailed

description of the sampling site can be found elsewhere (Lin et al. 2017). The measurement

campaign was conducted from 9 October to 4 November, 2016. The time for cloud events was

approximately 300 hours in the whole period. The ambient temperature varied from 4 to 21

degrees Celsius in this study (Figure S1), indicative of liquid-only clouds.

2.2 Instrumentation

Previous field measurement observed that median size of cloud/fog droplets was approximately

10 μm at the study region (Wu et al, 2004). Cloud droplets with an aerodynamics diameter

greater than 8 μm were collected using a GCVI inlet system (GCVI Model 1205, Brechtel

Manufacturing Inc.). The collected cloud droplets were dried using an evaporation chamber

(airflow temperature at 40 ℃) in the GCVI until only dry residual particles (cloud residues)

remained. To reliably guarantee the presence of cloud events, an upper-limit visibility threshold

of 5 km and a lower-limit relative humidity (RH) threshold of 95% were set in the GCVI

software (Bi et al., 2016; Lin et al., 2017). During precipitation periods, the GCVI automatically

shut down to protect against interference from raindrops. The particle transmission efficiency

of the cut size (8 μm) was 50% (Shingler et al., 2012). Due to the cloud droplets being

concentrated in the GCVI inlet, an enrichment factor was estimated to be 5.25 based on

theoretical calculations (Shingler et al., 2012). More detailed information about the GCVI has

been described in Bi et al. (2016). The number concentration of particles collected by the GCVI

was below 1 cm^3 during cloud-free periods, suggesting that instances of particle breakthrough

and small particle contamination were absent (Shingler et al., 2012). In addition, interstitial

135 particles were sampled using an inlet cyclone with a cut-off aerodynamic diameter of 2.5 μm

136 (PM$_{2.5}$ inlet) during cloudy episodes. The cloud residues had also been observed to be larger

137 size relative to the interstitial particles (Figure S2). Thus, it was proposed that the interstitial

138 particles had not already processed to become cloud droplet. During cloud-free episodes, the

139 PM$_{2.5}$ inlet was used to collect cloud-free particles. The measurement period of cloud residues,

140 interstitial particles, and cloud-free particles are shown in Figure S1.

141   The sampled cloud residues, interstitial particles, and cloud-free particles were subsequently

142 measured by a single particle aerosol mass spectrometer (SPAMS) (Hexin Analytical

143 Instrument Co., Ltd., Guangzhou, China) to obtain their size-resolved chemical composition.

144 Bipolar mass spectra of individual aerosol particles were obtained by the SPAMS. The

145 analytical method of the SPAMS has been described in Li et al. (2011). Briefly, the aerosol

146 particles are focused into a narrow particle beam and accelerated to a region where the vacuum

147 aerodynamic (d_{va}) size of the aerosol particles is measured using two continuous diode Nd:YAG

148 laser beams (532 nm). Based on the calculated velocity of the particles, a pulsed high power

149 laser (266 nm) can be precisely triggered to evaporate and ionize the particles. Production of

150 positive and negative ions are subsequently recorded using a dual-polarity time-of-flight mass

151 spectrometer. A specific mass-to-charge ratio (m/z) in the positive or negative mass spectrum

152 can correspond to the most probable chemical species dependent on prior field and lab studies.

153 The peak area of a specific m/z on individual particle is relevant to the mass of the corresponded

154 chemical species (Bhave et al., 2002; Pratt et al., 2011). Polystyrene latex spheres (Nanosphere

155 Size Standards, Duke Scientific Corp., Palo Alto) of 0.2-2.0 μm in diameter were used to

156 calibrate the sizes of the detected particles at the sampling site. It should be noted that particles

157　detected by the SPAMS mostly distribute in the size range of d_{va} 0.2-2.0 μm (Li et al., 2011).

158

159　**2.3 Screening of the Fe-containing aerosols**

160　During the sampling period, 154,862 cloud residues, 15,420 interstitial particles, and 168,427

161　cloud-free particles with d_{va} ranging between 0.2 and 2.0 μm were chemically analyzed with

162　the SPAMS. The Fe-containing aerosols typically had a positive ion peak at m/z 56. Since other

163　species, such as $[CaO]^+$, $[KOH]^+$, and $[C_3H_4O]^+$, may also contribute to m/z 56, the natural

164　isotopic composition of Fe ion peaks at both m/z 54 and 56 was chose to strengthen the

165　screening through excluding more ambiguous assignments (Zhang et al., 2014; Dall'Osto et al.,

166　2016). Furthermore, the known isotopic ratio of Fe ($^{56}Fe/^{54}Fe$ = 16) was used as an indicator

167　for Fe (Beard and Johnson, 1999). The ratio to identify the Fe-containing particles might be

168　below 16, due to organic peaks at m/z 54 and 56 in the Fe-containing particles. Considering the

169　varied ratio resulting from the matrix effect of laser desorption/ionization (Allen et al., 2000),

170　Furutani et al. (2011) performed a peak area ratio of m/z 56 to 54 above 3 to identify the Fe-

171　containing particles. However, the average single-particle mass spectra with a ratio of m/z 56

172　to 54 below 10 can also be obtained in the organic carbon particles (Zhang et al., 2014). A high

173　peak area ratio of m/z 56 to 54 above 10 was used in the present study, which had been applied

174　in the previous studies (Zhang et al., 2014; Dall'Osto et al., 2016) to minimize the interference

175　from other species. Thus, the Fe-containing particles in the study were identified by the

176　coexistence of peaks at m/z 56 and m/z 54, and a peak area ratio ($^{56}Fe/^{54}Fe$) above 10. The

177　errors were calculated assuming Poisson statistics for the analyzed particles in this work. A total

178　of 5,682 cloud droplet residues, 395 interstitial particles, and 5,086 cloud-free particles were

179 found to be internally mixed with Fe, representing 3.7 ± 0.1 % (by number), $2.6 \pm 0.1\%$, and

180 $3.0 \pm 0.1\%$ of the total measured cloud residues, interstitial particles, and cloud-free particles,

181 respectively. Because the low number of the collected Fe-containing cloud residues limited the

182 statistical analysis, the differences between single cloud events were not analyzed. Instead, an

183 average analysis covering all the cloud events was presented.

184 The Fe-containing aerosols, including cloud residues, interstitial particles, and cloud-free

185 particles, were initially grouped into 106 clusters using an adaptive resonance theory-based

186 neural network algorithm (ART-2a) with a vigilance factor of 0.8, learning rate of 0.05, and 20

187 iterations (Song et al., 1999). Then, by manually combining similar clusters, four primary types

188 of Fe-containing aerosols were obtained, including Fe-rich, Fe internally mixed with mineral

189 dust species (Fe-dust), Fe internally mixed with EC (Fe-EC), and Fe internally mixed with V

190 (Fe-V).

191

192 **3 Result and discussion**

193 **3.1 Characteristics and potential sources of the Fe-containing particle types**

194 The averaged single-particle mass spectra of the four Fe-containing types are shown in Figure

195 1. One common feature was that the four Fe-containing particle types were internally mixed

196 with secondary inorganic ions such as sulfate (m/z $-97[HSO_4]^-$) and/or nitrate (m/z $-46[NO_2]^-$

197 or $-62[NO_3]^-$). This suggests that the Fe-containing aerosols experienced atmospheric aging

198 processes during long-range transport.

199 The Fe-rich type exhibited the highest peak at m/z 56 Fe as well as sulfate and nitrate, which

200 was the largest fraction of Fe-containing particles, and contributed $84 \pm 1\%$ (by number), 78

201 $\pm$4%, and 81$\pm$1% to the Fe-containing cloud residues, interstitial particles, and cloud-free

202 particles, respectively (Figure 2). The crustal elements were rarely detected in the Fe-rich type,

203 suggesting a nonmineral dust source. The Fe-rich type was unlikely to be caused by biomass

204 burning sources due to the weak potassium (m/z 39[K]$^+$) peak (Bi et al. 2011). Lithium (m/z

205 7[Li]$^+$) was found to account for 7$\pm$1% (by number) of the Fe-rich type, implying a partial

206 contribution from fly ash as suggested by Furutani et al. (2011). Zhang et al. (2014) considered

207 that the Fe-rich particles were mostly produced by the iron/steel industry from Shanghai in

208 eastern China. In this study, a steel production site with an annual yield of 6.5 million tons was

209 located approximately 60 km east of the sampling site. The Fe-rich type detected here was most

210 likely from industrial activities.

211   The Fe-dust type was mainly composed of mineral dust peaks including [Al]$^+$ (m/z 27), [Ca]$^+$

212 (m/z 40), [SiO$_3$]$^-$ (m/z -76), and [PO$_3$]$^-$ (m/z -79) (Figure 1), which accounted for 12$\pm$1% (by

213 number), 15$\pm$2%, and 12$\pm$1% of the Fe-containing cloud residues, interstitial particles, and

214 cloud-free particles, respectively (Figure 2). However, no clear enhanced NF of the Fe-dust

215 type was detected in particle size range of 1.0-2.0 μm relative to 0.2-1.0 μm (14$\pm$1% versus

216 12$\pm$2 %, by number) (Figure S3). The large Fe-dust particles (above 2.0 μm) might have

217 already been deposited during transport. In addition, the Fe-dust particles may have a larger

218 size (above 2.0 μm) that could not be detected by the SPAMS.

219   The Fe-EC type was characterized by EC cluster ions (e.g., m/z $\pm$12[C]$^{+/-}$, $\pm$24[C$_2$]$^{+/-}$, $\pm$

220 [36C$_3$]$^{+/-}$, $\pm$48[C$_4$]$^{+/-}$, $\pm$[60C$_5$]$^{+/-}$) as well as strong sulfate (Figure 1). The internal mixture

221 of Fe-containing particles with EC was also observed in the Asian outflow atmosphere, mainly

222 due to the contribution from fossil fuel combustion in China (Furutani et al., 2011). The Fe-V

223 type showed the intense $[Fe]^+$ and $[V]^+$ (m/z 51) or vanadium oxide (m/z 67$[VO]^+$) peaks

224 (Figure 1). The Fe-V type was possibly related to residual fuel oil combustion sources, such as

225 ships and refineries (Furutani et al., 2011; Zhang et al., 2014; Dall'Osto et al., 2016). The Fe-

226 EC and Fe-V types were minor contributors (below $5\pm1\%$, by number) in this study (Figure

227 2).

228

3.2 The impact of cloud processing on secondary inorganic species in the Fe-containing

230 **cloud residues**

231 Sulfate, nitrate, chloride, and ammonium were the most common secondary inorganic species

232 produced by aqueous reactions. Comparisons of these secondary inorganic species between Fe-

233 containing cloud residues, interstitial particles and cloud-free particles showed the impact of

234 cloud processing or aqueous phases on the formation of these species associated with Fe-

235 containing particles. Comparisons during daytime (local time 0800-1900) and nighttime (local

236 time 2000-0700) were also performed to investigate the irradiation effect. The ambient

237 temperature showed a typically diurnal pattern. However, RH had a high value (nearly 100%)

238 during daytime when the cloud events exited. Note that variation in the meteorological

239 conditions may influence the comparisons. Due to the low number of particles detected, the Fe-

240 EC and Fe-V particle types were not analyzed in this section.

241   The number fractions (NFs) of sulfate in the Fe-containing cloud residues ($93\pm1\%$, by

242 number) and interstitial particles ($92\pm4\%$) were similar to those in the cloud-free particles (96

243 $\pm1\%$), as shown in Figure 3. The NFs of sulfate in the non-Fe cloud residues and interstitial

244 particles were also not observed to enhance relative to the non-Fe cloud-free particles ($87\pm1\%$

245   or 88±1% versus 92±1%, by number). Several field studies also failed to find the increased

246   NF or mass fraction of sulfate in cloud residues or interstitial particles (Drewnick et al., 2007;

247   Twohy and Anderson, 2008; Schneider et al., 2017). The cause for these observations remained

248   unknown. In this study, an extremely high NF (above 90%) of sulfate was measured in the Fe-

249   containing cloud-free particles, which makes it hard to find the minor changes after the particles

250   experienced cloud events. It was worth noting that the Fe-containing particles might experience

251   one or more cloud processes prior to arrival at the observed site, wherein sulfate may have

252   accumulated on the Fe-containing particles. Low SO_2 level (below 5 ppb) in the observed site

253   may also limit the formation of sulfate. Thus, we speculated that the contribution from the in-

254   cloud formation of sulfate was relatively small compared to the total amount of sulfate in the

255   Fe-containing cloud-free particles in this study.

256   The NFs of nitrate in the Fe-containing cloud residues (86 ±1 %, by number) and interstitial

257   particles (89 ±5%) were enhanced in comparison to the cloud-free particles (76 ±1%) (Figure

258   3). The enhanced NF of nitrate during cloud processing can be attributed to the partitioning

259   from gaseous HNO_3 into the aqueous phase and/or the heterogeneous reaction of N_2O_5 (Hayden

260   et al., 2008; Chang et al., 2011; Schneider et al., 2017). Photochemical reactions probably

261   played a vital role in nitrate formation (Pathak et al., 2009), leading to the increased NF of

262   nitrate in the Fe-containing cloud-free particles during daytime (Figure 4b). However, in the

263   case of the Fe-containing cloud residues, there was no distinct change in NF of nitrate between

264   daytime and nighttime (Figure 4b), reflecting that the in-cloud formation of nitrate was less

265   affected by photochemical reactions. The NF of nitrate in the Fe-dust cloud residues was higher

266   than that in the Fe-rich cloud residues (92 ±3% versus 86 ±1%, by number), despite a similar

267   NF of nitrate observed in the two Fe-containing cloud-free particle types (Figure 4b). This can

268   be explained by the fact that gaseous HNO_3 would be neutralized upon reaction with alkaline-

269   rich (e.g., Ca) particles in the Fe-dust cloud residues during cloud processing (Matsuki et al.,

270   2010).

271   Higher NFs of chloride were found in the Fe-containing cloud residues and interstitial

272   particles compared to the cloud-free particles (16 ±1% or 13 ±2% versus 6 ±1%, by number)

273   (Figure 3). The partitioning of volatile gaseous chloride (i.e., HCl) into the aqueous phase was

274   a major contributor to the increased chloride in cloud droplets (Sellegri et al., 2003). The

275   enhanced NF of chloride during cloud processing was unlikely to have resulted from the

276   invasion of sea salt particles, because 0.40 ±0.01 % (by number) of the Fe-containing cloud

277   residues was found to internally mix with the related sea salt peaks (e.g., m/z 81 $[Na_2{}^{35}Cl]^+$ or

278   83 $[Na_2{}^{37}Cl]^+$). Only 115 sea salt particles were obtained in the Non-Fe cloud residues,

279   suggesting less gaseous HCl was released from aged sea salt particles during cloud processing.

280   Recently, Fu et al. (2018) reported that the anthropogenic gaseous HCl emission was estimated

281   to be in a range from 20-200 kg/km^2 in southern China, mostly from coal burning, agricultural

282   biomass burning and waste incineration. The gaseous HCl sources in this region might originate

283   from regional transport of these anthropogenic HCl in southern China. The irradiation effect

284   during daytime would generally result in the reduction of ammonium chloride in the particles

285   due to evaporation at high temperature (Huang et al., 2011). In this study, there was no change

286   in NF of chloride in the Fe-containing cloud residues between daytime and nighttime (Figure

287   4c), suggesting that the amount of in-cloud chloride formation was less affected by irradiation

288   effect. In the case of cloud-free events, no decreased NF of chloride in the Fe-containing cloud-

289   free particles was also observed during daytime relative to the nighttime (Figure 4c),

290   presumably due to the formation of calcium chloride (Sullivan et al., 2007b). A significant

291   feature was also found in that the NF of chloride in the Fe-dust cloud residues was much higher

292   than that in the Fe-rich cloud residues ($45 \pm 3\%$ versus $12 \pm 1\%$, by number) (Figure 4c).

293   Relative to sulfate and nitrate, chloride showed a highly internally mixed state with Ca particles

294   (Figure S4), indicating that the Ca-rich particles in the Fe-dust cloud residues were responsible

295   for the in-cloud formation of chloride. Despite lower amounts ($13 \pm 1\%$, by number) of Ca

296   particles in the Fe-rich cloud residues, the enhanced NF of chloride was obvious (Figure 4c).

297   This was likely attributed to the uptake of volatile gaseous chloride (i.e., HCl) over simple

298   physical sorption due to the high water solubility of gaseous HCl (Sellegri et al., 2003).

299   The NFs of ammonium in the Fe-containing cloud residues ($35 \pm 1\%$, by number) and

300   interstitial particles ($34 \pm 3\%$) were analogous to those in the cloud-free particles ($30 \pm 1\%$)

301   (Figure 3). During nighttime, the significantly increased NF of ammonium in the Fe-containing

302   cloud residues was observed as compared to the cloud-free particles, especially for the Fe-dust

303   type ($35 \pm 1\%$ versus $20 \pm 1\%$, by number) (Figure 4d). Most ammonium in the Fe-dust cloud

304   residues was internally mixed with sulfate and/or nitrate. The secondary acids accumulated on

305   the Fe-Dust cloud residues might be a sink for NH_3 (Sullivan et al., 2007a; Nie et al., 2012).

306   During daytime, the increased NF of ammonium in the Fe-dust cloud-free particles was likely

307   attributed to the enhanced NFs of ammonium nitrate. This process might lead to a minor change

308   in the NF of ammonium between the Fe-dust cloud residues and cloud-free particles during

309   daytime.

310

3.3 The impact of cloud processing on oxalate precursors and oxalate in the Fe-containing cloud residues

The aqueous oxidation pathway of organic precursors was an important contributor to the in-cloud formation of oxalate (Sorooshian et al., 2007; Zhang et al., 2017b). Acetate (at m/z -59 $[C_2H_3O_2]^-$), methylglyoxal (m/z -71 $[C_3H_3O_2]^-$), glyoxylate (m/z -73 $[C_2HO_3]^-$), pyruvate (m/z -87 $[C_3H_3O_3]^-$), malonate (m/z -103 $[C_3H_3O_4]^-$), and succinate (m/z -117 $[C_4H_5O_4]^-$) had been suggested as the main precursors for the formation of oxalate in the atmospheric aqueous phase (Ervens et al., 2004; Lim et al., 2005; Sorooshian et al., 2006). A peak at m/z -59 might also be originated from the presence of $[HCNO_2]^-$ or levoglucosan (Bi et al., 2011). Increased NFs of the precursors were clearly identified in the Fe-containing cloud residues (38 $\pm1\%$, by number) and interstitial particles (35 $\pm3\%$) compared to cloud-free particles (26 $\pm1\%$) (Figure 3). These findings indicate the contribution of cloud processing to the formation of oxalate precursors. Photochemical reactions were another major pathway to form oxalate precursors (Kawamura and Bikkina, 2016). Although enhanced NF of the oxalate precursors was observed in the Fe-containing cloud-free particles during daytime, no variation in NF of the oxalate precursors was found in the Fe-containing cloud residues during either daytime or nighttime (Figure 4e). Therefore, the in-cloud formation of the oxalate precursors is less likely to be influenced by photochemical reactions. Interestingly, these precursors presented in 62 $\pm2\%$ (by number) of the Fe-dust cloud residues, which was much higher than 35 $\pm1\%$ (by number) of the Fe-rich cloud residues (Figure 4e). A similar trend was also found during the cloud-free periods (43 $\pm$ 2% versus 23 $\pm1\%$, by number) (Figure 4e). These findings suggest that the oxalate precursors would readily enrich in the Fe-dust particles.

16

333   The NFs of oxalate in the Fe-containing cloud residues ($45 \pm 1\%$, by number) and interstitial

334   particles ($38 \pm 3\%$) were higher than that in the cloud-free particles ($26 \pm 1\%$) (Figure 3).

335   Enhanced NFs of oxalate without its precursors were found for the Fe-containing cloud residues

336   ($15 \pm 1\%$, by number) and interstitial particles ($13 \pm 2\%$) in comparison to the cloud-free

337   particles ($10 \pm 1\%$) (Figure S5). This possibly resulted from gaseous oxalic acid partitioning

338   into cloud droplets (Sellegri et al., 2003). It should be mentioned here that such an enhancement

339   of oxalate may be related to other precursors (e.g., glutarate) that were not considered in this

340   study. On the other hand, oxalate that was internally mixed with its precursors accounted for 30

341   ± 1 % (by number) and $25 \pm 2\%$ of the Fe-containing cloud residues and interstitial particles,

342   respectively, which were much higher than the amount in the cloud-free particles ($16 \pm 1\%$)

343   (Figure S5). This result indicates that the presence of oxalate precursors would enhance the in-

344   cloud formation of oxalate, mostly via the aqueous oxidation of oxalate precursors (Ervens et

345   al., 2004; Sorooshian et al., 2006). Compared with the Fe-rich cloud residues, the higher NF of

346   oxalate in the Fe-dust cloud residues (Figure 4f) might be related to the plentiful precursors in

347   the Fe-dust cloud residues (Figure 4e). A lower NF of oxalate in the Fe-containing cloud

348   residues was measured during daytime relative to nighttime, indicating the photolysis of Fe-

349   oxalate complexes (Figure 4f). This phenomenon differed greatly from the in-cloud formation

350   of nitrate, chloride, and oxalate precursors in that their NF had no obvious change during both

351   daytime and nighttime. The lower NF of oxalate in the Fe-containing cloud residues during

352   daytime also implies that the photolysis of Fe-oxalate complexes could overwhelm the in-cloud

353   formation of oxalate during the day.

354   The Fenton reaction ($Fe^{2+} + H_2O_2 \rightarrow Fe^{3+} + OH^- + \cdot OH$) would yield OH-radicals, which

355 promote the conversion of the precursors to oxalate during cloud processing (Lim et al., 2010).

356 Higher NF of oxalate in the Fe-containing cloud residues was compared with the non-Fe cloud

357 residues (45 ±1% versus 7 ±1%, by number) (Figure S6). Moreover, a peak area ratio of oxalate

358 to its precursors was enhanced in the Fe-containing cloud residues relative to non-Fe cloud

359 residues (Figure 5a). These findings implies that aqueous-phase OH were likely produced by

360 redox cycling of the Fe-driven Fenton reaction (Hems et al., 2017), and thus enhance oxidation

361 of various precursors to form oxalate during cloud processing. Sorooshian et al. (2007)

362 observed that oxalate was more efficiently produced from aqueous oxidation of glyoxylate with

363 higher cloud liquid water content, corresponding to higher cloud droplet pH values. Relative to

364 Fe-containing interstitial particles, an increased peak area ratio of oxalate to its precursors in

365 the cloud residues (Figure 5a) might be due to their higher liquid water content. Moreover, in

366 the presence of ammonium, the peak area ratio of oxalate to its precursors was also enhanced

367 in the Fe-containing cloud residues (Figure S7). The enhanced peak area ratio of oxalate to its

368 precursors in the Fe-dust cloud residues at night was likely due to the enhancement of

369 ammonium (Figure 5b). Furthermore, nearly 90 ± 3% (by number) of oxalate in the Fe-dust

370 cloud residues was found to be internally mixed with ammonium during nighttime. Ortiz-

371 Montalvo et al. (2013) considered that the formation of ammonium oxalate would substantially

372 reduce the vapor pressure of oxalate, enhancing the yield of oxalate during cloud processing.

373 During the daytime, the decreased peak area ratio of oxalate to its precursors mostly resulted

374 from the degradation of oxalate associated with photolysis of Fe-oxalate complexes.

375

376 **3.4 Mixing state of the Fe-containing cloud residues**

377   Figure 6 displays the NF of various species in the four Fe-containing cloud residual types.

378   Abundant sulfate was found in the Fe-rich (94 $\pm$ 1%, by number), Fe-dust (85 $\pm$ 4%), Fe-EC

379   (92 $\pm$ 10%), and Fe-V (98 $\pm$ 8%) cloud residues. Substantial sulfate in the Fe-containing

380   particles was also observed over East Asia (Furutani et al., 2011; Moffet et al., 2012; Li et al.,

381   2013). Despite no significantly increased NF of sulfate in Fe-containing particles during cloud

382   processing, the substantial sulfate observed here was expected due to the likely high levels of

383   SO_2 encountered during long-distance transport. High amounts (above 80%, by number) of

384   nitrate were observed in the Fe-containing cloud residues except for the Fe-EC type (59 $\pm$ 8%).

385   However, a relatively high NF of ammonium was obtained in the Fe-EC cloud residues (62 $\pm$

386   8%, by number) compared to the other Fe-containing cloud residual types (below 45 %).

387   Approximately 97 $\pm$ 1% (by number) and 54 $\pm$ 5% of ammonium were found to internal mix

388   sulfate and nitrate respectively in the Fe-EC type, suggesting that ammonium in the Fe-EC

389   cloud residues has a more contribution from ammonium sulfate rather than ammonium nitrate.

390   It should be noted here that the evaporation chamber of the GCVI may lead to a depletion of

391   ammonium nitrate in the Fe-EC cloud residues (Hayden et al., 2008). The higher NF of chloride

392   was found in the Fe-dust cloud residues (45 $\pm$ 3%, by number) relative to the other Fe-

393   containing cloud residual types (below 15%). As discussed above, the Ca-rich particles in the

394   Fe-dust type contributed considerably to the in-cloud formation of chloride. Oxalate accounted

395   for 45 $\pm$ 1% (by number), 51 $\pm$ 3%, and 50 $\pm$ 6 % of the Fe-rich, Fe-dust, and Fe-V cloud

396   residues, respectively, which was much higher than the oxalate found in Fe-EC cloud residues

397   (19 $\pm$ 4%). The less NF of oxalate in the Fe-EC cloud residues might be restricted by the low

398   NF of the oxalate precursors.

399

4 Conclusions and atmospheric implications

Previous laboratory and modeling studies focused on the cloud processing of Fe-containing

particles from dust sources (Hand et al., 2004; Mahowald et al., 2005; Shi et al., 2009). Several

modeling and field studies argued that the combustion Fe sources should be taken into account

over East Asia (Luo et al., 2008; Furutani et al., 2011; Moffet et al., 2012; Zhang et al., 2014;

Ito, 2015). This study includes the first report of the abundant Fe-rich particles related to the

participation of combustion sources in cloud processing over East Asia.

Luo et al. (2008) performed a modeling calculation to estimate the influence of atmospheric

process on soluble Fe by assuming that cloud processing had sufficient acidic species to process

more Fe soluble. However, they did not definite the specific acid types. In the current study, the

enhanced NFs of nitrate and chloride in the Fe-containing particles was produced via

partitioning and heterogeneous/aqueous chemistry of gaseous HNO_3 and HCl or other

precursors. More importantly, the in-cloud formation of nitrate and chloride was enhanced in

the Fe-dust type relative to the Fe-rich type. Laboratory studies also showed that Fe dissolution

in the HCl solution differed from that in the H_2SO_4 and HNO_3 solutions (Fu et al., 2010;

Rubasinghege et al., 2010). In order to accurately predict bioavailable Fe during cloud

processing, the impact of different acids on Fe dissolution in varied Fe types might be

considered for future modeling study.

Modeling calculations showed that relative to proton-promoted Fe dissolution, the addition

of oxalate accompanied with photolysis of Fe-oxalate complexes in aqueous chemistry more

than doubled the soluble Fe deposition from combustion sources in global oceanic regions (Ito,

20

421 2015). Our data showed that aqueous-phase oxidation of the oxalate precursors was an

422 important contributor to the in-cloud formation of oxalate in the Fe-rich particles. The Fe-driven

423 Fenton reaction likely accelerate the conversion of the oxalate precursors to oxalate in the Fe-

424 rich particles during cloud processing. Moreover, the complexation of Fe with oxalate might

425 further increase oxalate content in the Fe-rich cloud residues (Chen and Grassian, 2013).

426 Ammonium species possibly enhance oxidation of precursors to form oxalate in the Fe-rich

427 cloud residues through increasing aerosol pH. On the other hand, the photolysis of Fe-oxalate

428 complexes in the Fe-rich cloud residues would lead to the losses of oxalate during daytime.

429 These results supported the role of oxalate in aqueous chemistry in soluble Fe deposition from

430 combustion sources. However, the modeling study assumed that oxalate entirely mixed with

431 Fe-containing particles from combustion sources in the bulk aqueous phase (Ito, 2015). In this

432 work, nearly $45 \pm 1\%$ (by number) of the Fe-rich cloud residues contained only oxalate. The

433 mass concentration of oxalate in the bulk aqueous phase might be overestimated in model

434 simulations. This might suppress Fe dissolution under low concentration of oxalate because of

435 competition of oxalate complexation between dissolved Fe in solution and Fe on the particle

436 surface (Chen and Grassian, 2013).

437

444   132744KYSB20160036).

445

446   **References**

447   Abbaspour, N., Hurrell, R., and Kelishadi, R.: Review on iron and its importance for human

448   health, J. Res. Med. Sci., 19, 164-174, 2014.

449   Allen, J.O., Fergenson, D.P., Gard, E.E., Hughes, L.S., Morrical, B.D., Kleeman, M.J., Gross,

450   D.S., Galli, M.E., Prather, K.A., and Cass, G.R.: Particle detection efficiencies of aerosol

451   time of flight mass spectrometers under ambient sampling conditions, Environ. Sci.

452   Technol. 34, 211-217, https://doi.org/10.1021/es9904179, 2000.

453   Beard, B. L., and Johnson, C. M.: High precision iron isotope measurements of terrestrial and

454   lunar   materials,   Geochim.   Cosmochim.   Acta,   63,   1653-1660,

455   https://doi.org/10.1016/S0012-821X(01)00581-7, 1999.

456   Bhave, P.V., Allen, J.O., Morrcal, B.D., Fergenson, D.P., Cass, G.R., and Prather, K. A.: A field-

457   based approach for determining atofms instrument sensitivities to ammonium and nitrate,

458   Environ. Sci. Technol., 36, 4868-4879, https://doi.org/10.1021/es015823i, 2002.

459   Bi, X., Lin, Q., Peng, L., Zhang, G., Wang, X., Brechtel, F.J., Chen, D., Li, M., Peng, P.A.,

460   Sheng, G., and Zhou, Z.: In situ detection of the chemistry of individual fog droplet

461   residues in the Pearl River Delta region, China, J. Geophys. Res. Atmos., 121, 9105-9116,

462   https://doi.org/10.1002/2016JD024886, 2016.

463   Bi, X., Zhang, G., Li, L., Wang, X., Li, M., Sheng, G., Fu, J., and Zhou, Z.: Mixing state of

464   biomass burning particles by single particle aerosol mass spectrometer in the urban area

465   of   PRD,   China,   Atmos.   Environ.,   45,   3447-3453,

466   https://doi.org/10.1016/j.atmosenv.2011.03.034, 2011.

467   Chang, W.L., Bhave, P.V., Brown, S.S., Riemer, N., Stutz, J., and Dabdub, D.: Heterogeneous

468   atmospheric chemistry, ambient measurements, and model calculations of N_2O_5: A review,

469   Aerosol Sci. Tech., 45, 665-695, https://doi.org/10.1080/02786826.2010.551672, 2011.

470   Chen, H., and Grassian, V. H.: Iron dissolution of dust source materials during simulated acidic

471   processing: The effect of sulfuric, ascetic, and oxalic acids, Environ. Sci. Technol., 47,

472   10312-10321, https://doi.org/10.1021/es401285s, 2013.

473   Cheng, C., Li, M., Chan, C.K., Tong, H., Chen, C., Chen, D., Wu, D., Li, L., Wu, C., Cheng, P.,

474   Gao, W., Huang, Z., Li, X., Zhang, Z., Fu, Z., Bi, Y., and Zhou, Z.: Mixing state of oxalic

475   acid containing particles in the rural area of Pearl River Delta, China: implications for the

476   formation   mechanism   of   oxalic   acid,   Atmos.   Chem.   Phys.,   17,   9519-9533,

477   https://doi.org/10.5194/acp-17-9519-2017, 2017.

478   Costa, D.L., and Dreher, K.L.: Bioavailable transition metals in particulate matter mediate

479   cardiopulmonary injury in healthy and compromised animalmodels, Environ. Health

480   Perspect., 105, 1053-1060, https://doi.org/10.1289/ehp.97105s51053, 1997.

481   Dall'Osto, M., Beddows, D.C., Harrison, R.M., and Onat, B.: Fine iron aerosols are internally

482   mixed with nitrate in the urban European atmosphere, Environ. Sci. Technol., 50, 4212-

483   4220, https://doi.org/10.1021/acs.est.6b01127, 2016.

484   Deguillaume, L., Leriche, M., Desboeufs, K., Mailhot, G., George, C., and Chaumerliac, N.:

485   Transition   metals   in   atmospheric   liquid   phases: Sources,   reactivity,   and   sensitive

486   parameters, Chem. Rev., 105, 3388-3431, https://doi.org/10.1021/cr040649c, 2005.

487   Drewnick, F., Schneider, J., Hings, S.S., Hock, N., Noone, K., Targino, A., Weimer, S., and

488   Borrmann, S.: Measurement of ambient, interstitial, and residual aerosol particles on a

489   mountaintop site in central Sweden using an aerosol mass spectrometer and a CVI, J.

490   Atmos. Chem., 56, 1-20, https://doi.org/10.1007/s10874-006-9036-8, 2007.

491 Ervens, B., Feingold, G., Frost, G. J., and Kreidenweis, S. M.: A modeling study of aqueous

492   production of dicarboxylic acids: 1. chemical pathways and speciated organic mass

493   production,   J.   Geophys.   Res.   Atmos.,   109,   D15205,

494   https://doi.org/10.1029/2003JD004387, 2004.

495 Ervens, B., Turpin, B., and Weber, R.: Secondary organic aerosol formation in cloud droplets

496   and aqueous particles (aqSOA): a review of laboratory, field and model studies, Atmos.

497   Chem. Phys., 11, 11069-11102, https://doi.org/10.5194/acp-11-11069-2011, 2011.

498 Fomba, K.W., Müller, K., Van Pinxteren, D., and Herrmann, H.: Aerosol size-resolved trace

499   metal composition in remote northern tropical Atlantic marine environment: case study

500   Cape Verde islands, Atmos. Chem. Phys., 13, 4801-4814, https://doi.org/10.5194/acp-13-

501   4801-2013, 2013.

502 Fu, H., Cwiertny, D. M., Carmichael, G. R., Scherer, M. M., and Grassian, V. H.: Photoreductive

503   dissolution of Fe-containing mineral dust particles in acidic media, J. Geophys. Res.

504   Atmos., 115, D11304, https://doi.org/ 10.1029/2009JD012702, 2010.

505 Fu, X., Wang, T., Wang, S., Zhang, L., Cai, S., Xing, J., and Hao, J.: Anthropogenic emissions

506   of hydrogen chloride and fine particulate chloride in China, Environ. Sci. Technol., 52,

507   1644-1654, https://doi.org/10.1021/acs.est.7b05030, 2018.

508 Furutani, H., Jung, J., Miura, K., Takami, A., Kato, S., Kajii, Y., and Uematsu, M.: Single-

509   particle chemical characterization and source apportionment of iron-containing

atmospheric aerosols in Asian outflow, J. Geophys. Res. Atmos., 116, D18204, https://doi.org/10.1029/2011JD015867, 2011.

Hand, J.L., Mahowald, N. M., Chen, Y., Siefert, R.L., Luo, C., Subramaniam, A., and Fung, I.: Estimates of atmospheric-processed soluble iron from observations and a global mineral aerosol model: biogeochemical implications, J. Geophys. Res. Atmos., 109, D17205, https://doi.org/10.1029/2004JD004574, 2004.

Harris, E., Sinha, B., van Pinxteren, D., Tilgner, A., Fomba, K.W., Schneider, J., Roth, A., Gnauk, T., Fahlbusch, B., Mertes, S., Lee, T., Collett, J., Foley, S., Borrmann, S., and Herrmann., H.: Enhanced role of transition metal ion catalysis during in-cloud oxidation of SO_2, Science, 340, 727-730, https://doi.org/10.1126/science.1230911, 2013.

Hayden, K.L., Macdonald, A.M., Gong, W., Toom-Sauntry, D., Anlauf, K.G., Leithead, A., Li, S.M., Leaitch, W.R., and Noone, K.: Cloud processing of nitrate, J. Geophys. Res. Atmos., 113, D18201, https://doi.org/10.1029/2007JD009732, 2008.

Hems, R.F., Hsieh, J.S., Slodki, M.A., Zhou, S., and Abbatt, J. P.: Suppression of OH generation from the Photo-Fenton reaction in the presence of α-Pinene secondary organic aerosol material, Environ. Sci. Technol. Lett., 410, 439-443, https://doi.org/10.1021/acs.estlett.7b00381, 2017.

Huang, X.F., He, L.Y., Hu, M., Canagaratna, M.R., Kroll, J.H., Ng, N.L., Zhang, Y.H., Lin, Y., Xue, L., Sun, T.L., Liu, X.G., Shao, M., Jayne, J.T., and Worsnop, D.R.: Characterization of submicron aerosols at a rural site in Pearl River Delta of China using an Aerodyne High-Resolution Aerosol Mass Spectrometer, Atmos. Chem. Phys., 11, 1865-1877, https://doi.org/10.5194/acp-11-1865-2011, 2011.

Ito, A.: Atmospheric processing of combustion aerosols as a source of bioavailable iron, Environ. Sci. Technol. Lett., 2, 70-75, https://doi.org/10.1021/acs.estlett.5b00007, 2015.

Jickells, T.D., An, Z.S., Andersen, K.K., Baker, A.R., Bergametti, G., Brooks, N., Cao, J.J., Boyd, P.W., Duce, R.A., Hunter, K.A., Kawahata, H., Kubilay, N., LaRoche, J., Liss, P.S., Mahowald, N., Prospero, J.M., Ridgwell, A.J., Tegen, I., and Torres, R.: Global iron connections between desert dust, ocean biogeochemistry, and climate, Science, 308, 67-71, https://doi.org/10.1126/science.1105959, 2005.

Kawamura, K., and Bikkina, S.: A review of dicarboxylic acids and related compounds in atmospheric aerosols: molecular distributions, sources and transformation, Atmos. Res., 170, 140-160, https://doi.org/10.1016/j.atmosres.2015.11.018, 2016.

Li, L., Huang, Z., Dong, J., Li, M., Gao, W., Nian, H., Fu, Z., Zhang, G., Bi, X., and Cheng, P.: Real time bipolar time-of-flight mass spectrometer for analyzing single aerosol particles, Int. J. Mass Spectrom., 303, 118-124, https://doi.org/10.1016/j.ijms.2011.01.017, 2011.

Li, W., Wang, T., Zhou, S., Lee, S., Huang, Y., Gao, Y., and Wang, W.: Microscopic observation of metal-containing particles from Chinese continental outflow observed from a non-industrial site, Environ. Sci. Technol., 47, 9124-9131, https://doi.org/10.1021/es400109q, 2013.

Lim, H.J., Carlton, A.G., and Turpin, B.J.: Isoprene forms secondary organic aerosol through cloud processing: Model simulations, Environ. Sci. Technol., 39, 4441-4446, https://doi.org/10.1021/es048039h, 2005,

Lim, Y.B., Tan, Y., Perri, M.J., Seitzinger, S.P., and Turpin, B.J.: Aqueous chemistry and its role in secondary organic aerosol (SOA) formation, Atmos. Chem. Phys., 10, 10521-10539,

554   https://doi.org/10.5194/acp-10-10521-2010, 2010.

555 Lin, Q., Zhang, G., Peng, L., Bi, X., Wang, X., Brechtel, F.J., Li, M., Chen, D., Peng, P., Sheng,

556   G., and Zhou, Z.: In situ chemical composition measurement of individual cloud residue

557   particles at a mountain site, southern China, Atmos, Chem. Phys., 17, 8473-8488,

558   https://doi.org/10.5194/acp-17-8473-2017, 2017.

559 Luo, C., Mahowald, N., Bond, T., Chuang, P.Y., Artaxo, P., Siefert, R., Chen, Y., and Schauer,

560   J.: Combustion iron distribution and deposition, Global Biogeochem. Cycles, 22, GB1012,

561   https://doi.org/10.1029/2007GB002964, 2008.

562 Mahowald, N.M., Baker, A.R., Bergametti, G., Brooks, N., Duce, R. A., Jickells, T. ., Kubilay,

563   N., Prospero, J.M., and Tegen, I.: Atmospheric global dust cycle and iron inputs to the

564   ocean, Global Biogeochem. Cycles, 19, GB4025, https://doi.org/10.1029/2004GB002402,

565   2005.

566 Matsuki, A., Schwarzenboeck, A., Venzac, H., Laj, P., Crumeyrolle, S., and Gomes, L.: Cloud

567   processing of mineral dust: direct comparison of cloud residual and clear sky particles

568   during AMMA aircraft campaign in summer 2006, Atmos. Chem. Phys., 10, 1057-1069,

569   https://doi.org/10.5194/acp-10-1057-2010, 2010.

570 Moffet, R.C., Furutani, H., Rödel, T.C., Henn, T.R., Sprau, P.O., Laskin, A., Uematsu, M., and

571   Gilles, M.K.: Iron speciation and mixing in single aerosol particles from the Asian

572   continental   outflow,   J.   Geophys.   Res.   Atmos.,   117,   D07204,

573   https://doi.org/10.1029/2011JD016746, 2012.

574 Nie, W., Wang, T., Xue, L. K., and Ding, A. J.: Asian dust storm observed at a rural mountain

575   site in southern china: chemical evolution and heterogeneous photochemistry, Atmos.

576   Chem. Phys., 12, 11985-11995, https://doi.org/10.5194/acp-12-11985-2012, 2012.

577   Ortiz-Montalvo, D.L., Häkkinen, S.A.K., Schwier, A.N., Yong, B.L., Mcneill, V.F., and Turpin,

578   B. J.: Ammonium addition (and aerosol pH) has a dramatic impact on the volatility and

579   yield of glyoxal secondary organic aerosol, Environ. Sci. Technol., 48, 255-262,

580   https://doi.org/10.1021/es4035667, 2013.

581   Pathak, R. K., Wu, W. S., and Wang, T.: Summertime $PM_{2.5}$ ionic species in four major cities

582   of china: nitrate formation in an ammonia-deficient atmosphere, Atmos. Chem. Phys., 9,

583   1711-1722, https://doi.org/10.5194/acp-9-1711-2009, 2009.

584   Pratt, K.A., Murphy, S. M., Subramanian, R., Demott, P.J., Kok, G.L., Campos, T., Rogers,

585   D.C., Prenni, A.J., Heymsfield, A.J., Seinfeld, J.H., and Prather, K.A.: Flight-based

586   chemical characterization of biomass burning aerosols within two prescribed burn smoke

587   plumes, Atmos. Chem. Phys., 11, 12549-2565, https://doi:10.5194/acp-11-12549-2011,

588   2011.

589   Rubasinghege, G., Lentz, R.W., Scherer, M.M., and Grassian, V.H.: Simulated atmospheric

590   processing of iron oxyhydroxide minerals at low pH: roles of particle size and acid anion

591   in iron dissolution, P. Natl. Acad. Sci. USA, 107, 6628-6633,

592   https://doi.org/10.1073/pnas.0910809107, 2010.

593   Shi, Z., Krom, M.D., Bonneville, S., Baker, A.R., Jickells, T.D., and Benning, L.G.: Formation

594   of iron nanoparticles and increase in iron reactivity in mineral dust during simulated cloud

595   processing, Environ. Sci. Technol., 43, 6592-6596, https://doi.org/10.1021/es901294g,

596   2009.

597   Schneider, J., Mertes, S., van Pinxteren, D., Herrmann, H., and Borrmann, S.: Uptake of nitric

598   acid, ammonia, and organics in orographic clouds: mass spectrometric analyses of droplet

599   residual and interstitial aerosol particles, Atmos. Chem. Phys., 17, 1571-1593,

600   https://doi.org/10.5194/acp-17-1571-2017, 2017.

601 See, S.W., Wang, Y.H., and Balasubramanian, R.: Contrasting reactive oxygen species and

602   transition metal concentrations in combustion aerosols, Environ. Res., 103, 317-324,

603   https://doi.org/10.1016/j.envres.2006.08.012, 2007.

604 Sedwick, P.N., Sholkovitz, E.R., and Church, T.M.: Impact of anthropogenic combustion

605   emissions on the fractional solubility of aerosol iron: Evidence from the Sargasso Sea,

606   Geochem. Geophys. Geosyst., 8, Q10Q06, https://doi.org/10.1029/2007GC001586, 2007.

607 Sellegri, K., Laj, P., Marinoni, A., Dupuy, R., Legrand, M., and Preunkert, S.: Contribution of

608   gaseous and particulate species to droplet solute composition at the Puy de Dôme, France,

609   Atmos. Chem. Phys., 3, 1509-1522, https://doi.org/10.5194/acp-3-1509-2003, 2003.

610 Shingler, T., Dey, S., Sorooshian, A., Brechtel, F.J., Wang, Z., Metcalf, A., Coggon, M.,

611   Mülmenstädt, J., Russell, L.M., Jonsson, H.H., and Seinfeld, J.H.: Characterisation and

612   airborne deployment of a new counterflow virtual impactor inlet, Atmos. Meas. Tech., 5,

613   1259-1269, https://doi.org/10.5194/amt-5-1259-2012, 2012.

614 Song, X.H., Hopke, P.K., Fergenson, D.P., and Prather, K.A.: Classification of single particles

615   analyzed by ATOFMS using an artificial neural network, ART-2A, Anal. Chem., 71, 860-

616   865, https://doi.org/10.1021/ac9809682, 1999.

617 Sorooshian, A., Ng, N.L., Chan, A.W.H., Feingold, G., Flagan, R.C., and Seinfeld, J.H.:

618   Particulate organic acids and overall water-soluble aerosol composition measurements

619   from the 2006 Gulf of Mexico Atmospheric Composition and Climate Study (GoMACCS),

J. Geophys. Res. Atmos., 112, D13201, https://doi.org/10.1029/2007JD008537, 2007.

Sorooshian, A., Varutbangkul, V., Brechtel, F.J., Ervens, B., Feingold, G., Bahreini, R., Murphy, S.M., Holloway, J. S., Atlas, E.L., Buzorius,G., Jonsson, H., Flagan, R.C., and Seinfeld, J.H.: Oxalic acid in clear and cloudy atmospheres: analysis of data from international consortium for atmospheric research on transport and transformation 2004, J. Geophys. Res. Atmos., 111, D23S45, https://doi.org/10.1029/2005JD006880, 2006.

Sullivan, R., Guazzotti, S., Sodeman, D., and Prather, K.: Direct observations of the atmospheric processing of Asian mineral dust, Atmos. Chem. Phys., 7, 1213-1236, https://doi.org/10.5194/acp-7-1213-2007, 2007.

Sullivan, R., and Prather, K.: Investigations of the diurnal cycle and mixing state of oxalic acid in individual particles in Asian aerosol outflow, Environ. Sci. Tech., 41, 8062-8069, https://doi.org/10.1021/es071134g, 2007a.

Sullivan, R.C., Guazzotti, S.A., Sodeman, D.A., Tang, Y., Carmichael, G.R., and Prather, K.A.: Mineral dust is a sink for chlorine in the marine boundary layer, Atmos. Environ., 41, 7166-7179, https://doi.org/10.1016/j.atmosenv.2007.05.047, 2007b.

Tsai, I.C., Chen, J.P., Lin, P.Y., and Wang, W.C.: Sulfur cycle and sulfate radiative forcing simulated from a coupled global climate-chemistry model, Atmos. Chem. Phys., 10, 3693-3709, https://doi.org/10.5194/acp-10-3693-2010, 2010.

Twohy, C.H., and Anderson, J.R.: Droplet nuclei in non-precipitating clouds: composition and size matter, Environ. Res. Lett., 3, 045002, doi:10.1088/1748-9326/3/4/045002, 2008.

Wu, D., Deng, X.J., Ye,Y.X., and Mao, W.: The study of fog-water chemical composition in Dayaoshan of Nanling Mountain (in Chinese), Acta Meteorol. Sin., 62, 476-485, 2004.

642   Yang, F., Chen, H., Wang, X., Yang, X., Du, J., and Chen, J.: Single particle mass spectrometry

643   of oxalic acid in ambient aerosols in Shanghai: Mixing state and formation mechanism,

644   Atmos. Environ., 43, 3876-3882, https://doi.org/10.1016/j.atmosenv.2009.05.002, 2009.

645   Zhang, G., Bi, X., Lou, S., Li, L., Wang, H., Wang, X., Zhou, Z., Sheng, G., Fu, J., and Chen,

646   C.: Source and mixing state of iron-containing particles in Shanghai by individual particle

647   analysis, Chemosphere, 95, 9-16, https://doi.org/10.1016/j.chemosphere.2013.04.046,

648   2014.

649   Zhang, G., Lin, Q., Peng, L., Bi, X., Chen, D., Li, M., Li, L., Brechtel, F.J., Chen, J., Yan, W.,

650   Wang, X., Peng, P., Sheng, G., and Zhou, Z.: The single-particle mixing state and cloud

651   scavenging of black carbon: a case study at a high-altitude mountain site in southern China,

652   Atmos. Chem. Phys., 17, 14975-14985, doi:10.5194/acp-17-14975-2017, 2017a.

653   Zhang, G., Lin, Q., Peng, L., Yang, Y., Fu, Y., Bi, X., Li, M., Chen, D., Chen, J., Cai, Z., Wang,

654   X., Peng, P., Sheng, G., and Zhou, Z.: Insight into the in-cloud formation of oxalate based

655   on in situ measurement by single particle mass spectrometry, Atmos, Chem. Phys., 17,

656   13891-13901, doi:10.5194/acp-17-13891-2017, 2017b.

657   Zhang, X.Y., Gong, S.L., Arimoto, R., Shen, Z.X., Mei, F.M., Wang, D., and Cheng, Y.:

658   Characterization and temporal variation of Asian dust aerosol from a site in the northern

659   Chinese deserts, J. Atmos. Chem., 44, 241-257, https://doi.org/10.1023/A:1022900220357,

660   2003.

661   Figure captions:

662   Figure 1. The average single-particle mass spectra of the four Fe-containing types.
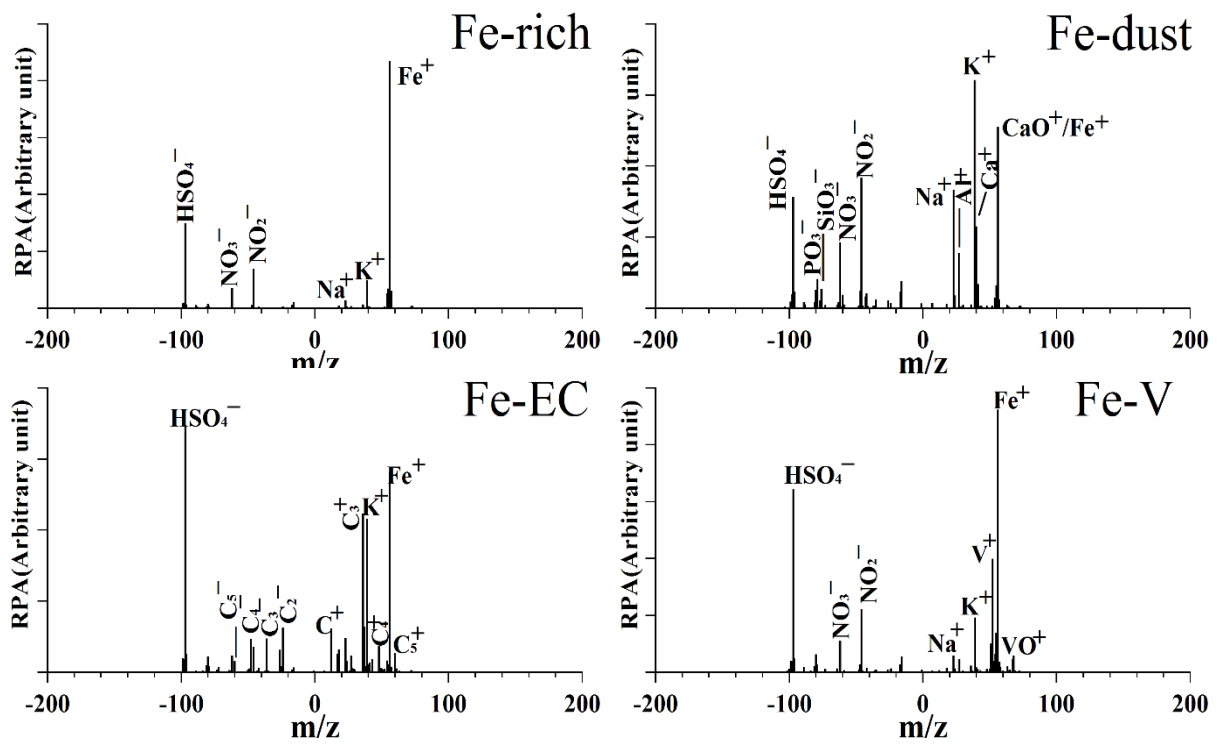
663   Figure 2. Number fraction of the four Fe-containing types in the Fe-containing cloud residues,

664   interstitial particles, and cloud-free particles during the whole study period.

665   Figure 3. Comparison in number fractions of sulfate (m/z -97), nitrate (m/z -46 or -62), chloride

666   (m/z -35 or -37), ammonium (m/z 18), oxalate precursors (m/z -59, -71, -73, -87, -103, or -117),

667   and oxalate (m/z -89) between the Fe-containing cloud residues, interstitial particles and cloud-

668   free particles.

669   Figure 4. Comparison in number fractions of sulfate (m/z -97), nitrate (m/z -46 or -62) , chloride

670   (m/z -35 or -37), ammonium (m/z 18) , oxalate precursors (m/z -59, -71, -73, -87, -103, or -

671   117), and oxalate (m/z -89) in the Fe-rich, Fe-dust, and all Fe-containing (total-Fe) types

672   between the cloud residues and cloud-free particles types and their difference during daytime

673   and nighttime. The comparison was not performed for the interstitial particles due to the low

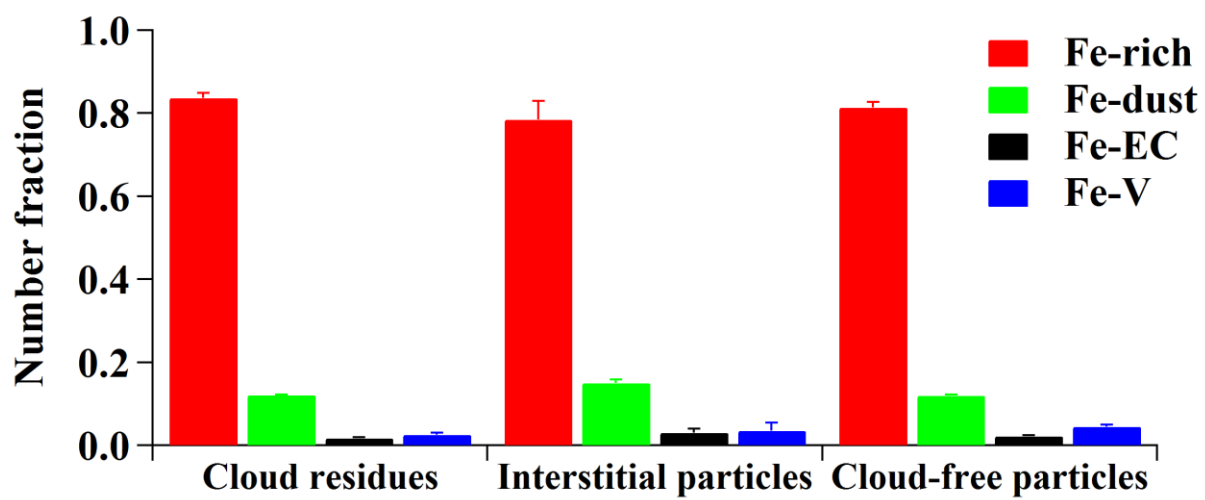674   number of detected particles.

675   Figure 5. Peak area ratio of oxalate (m/z -89) to the sum of the peak areas of its precursors

676   (m/z -59, -71, -73, -87, -103, or -117) in the total-Fe and non-Fe types (a); Peak area ratio of

677   oxalate to its precursors in the Fe-rich, Fe-dust, total-Fe and non-Fe types during daytime and

678   nighttime (b).

679   Figure 6. The number fractions of sulfate (m/z -97), nitrate (m/z -46 or -62), chloride (m/z -35

680   or -37), ammonium (m/z 18), oxalate (m/z -89), oxalate precursors (m/z -59 , -71, -73, -87, 103,

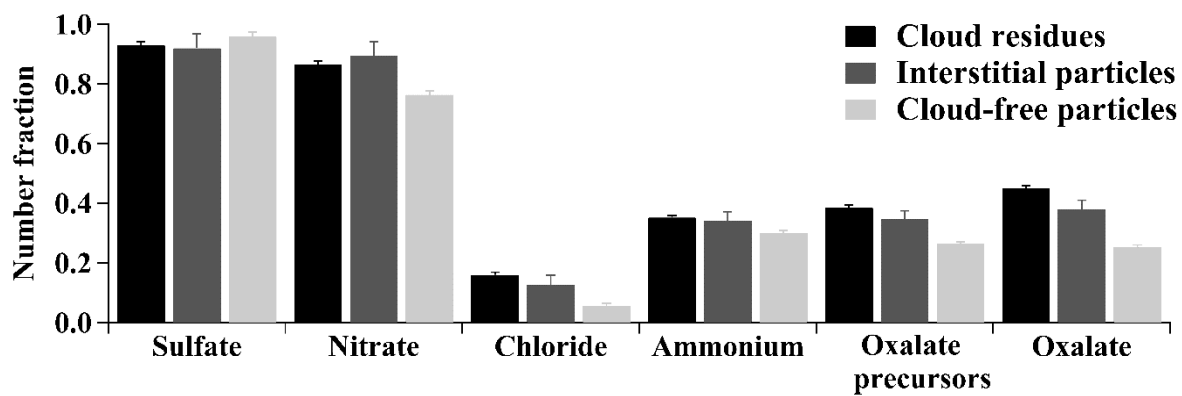681   or -117), Ca (m/z 40), and $[SiO_3]^-$ (m/z -76) in the four Fe-containing cloud residues.
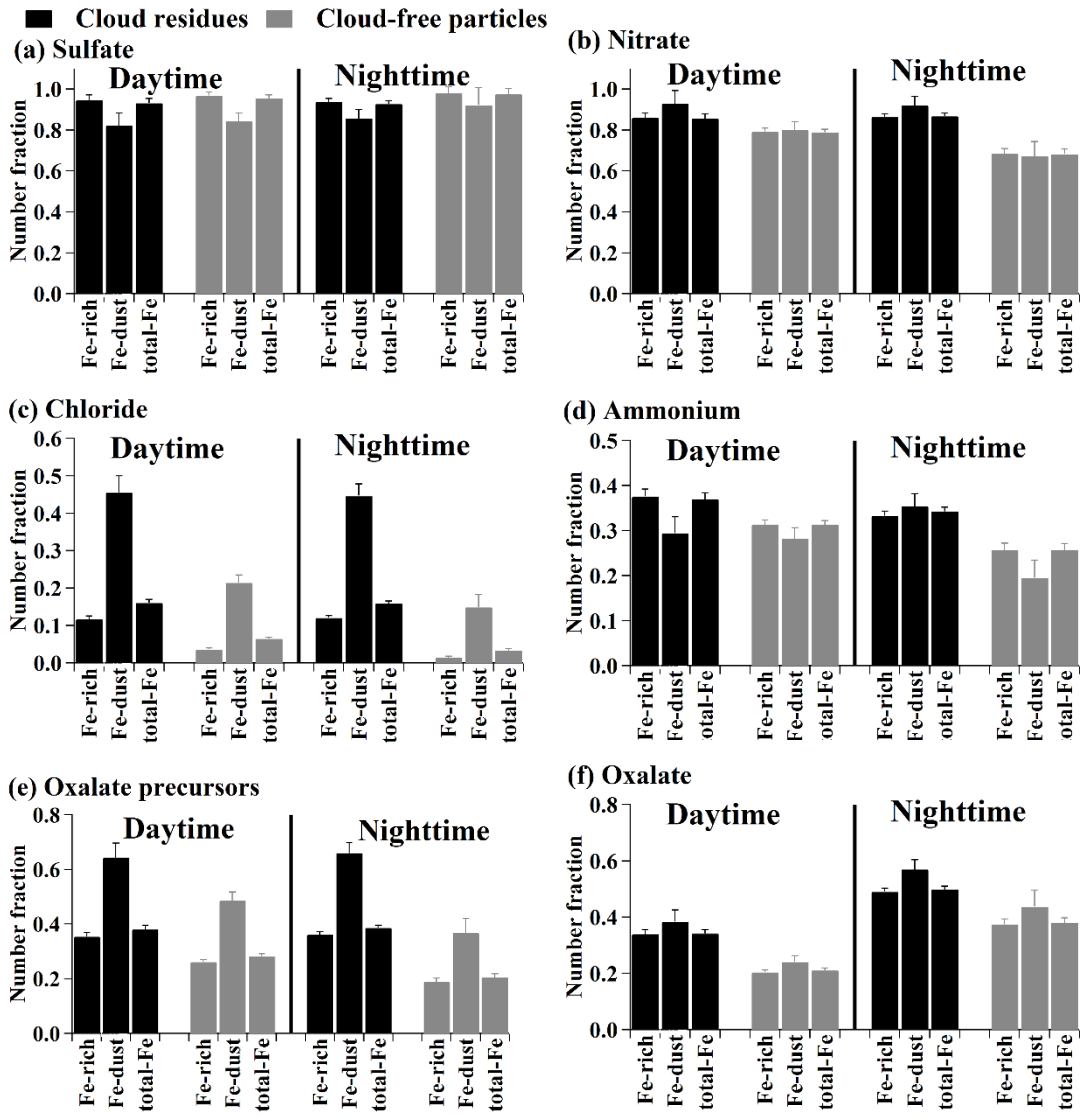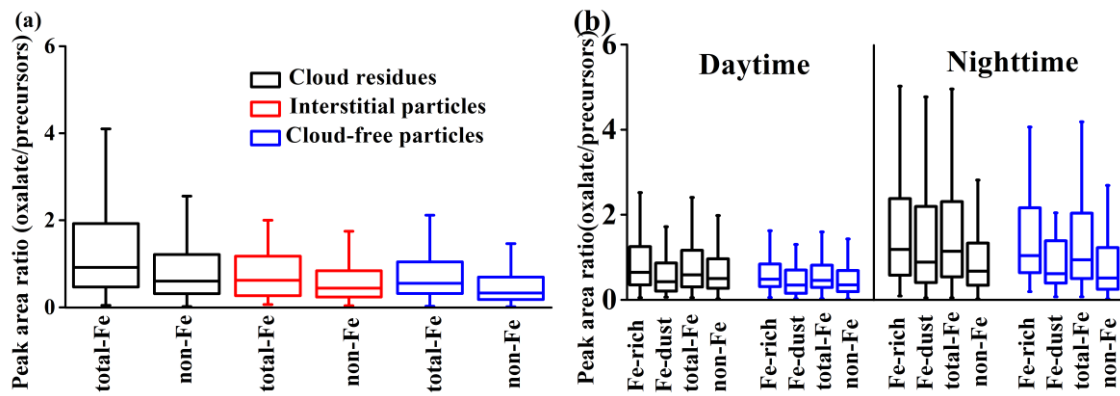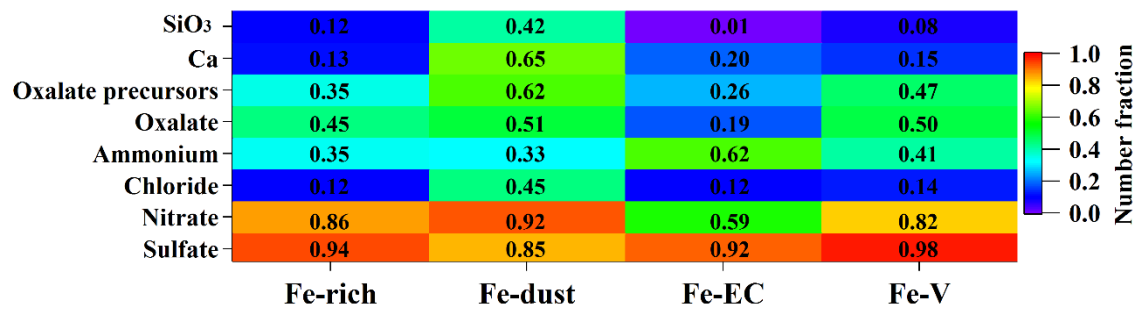
682

Figure 1.

684

685   Figure 2.

686

687   Figure 3.

688

689   Figure 4.

690

691   Figure 5.

692

	Fe-rich	Fe-dust	Fe-EC	Fe-V
SiO$_3$	0.12	0.42	0.01	0.08
Ca	0.13	0.65	0.20	0.15
Oxalate precursors	0.35	0.62	0.26	0.47
Oxalate	0.45	0.51	0.19	0.50
Ammonium	0.35	0.33	0.62	0.41
Chloride	0.12	0.45	0.12	0.14
Nitrate	0.86	0.92	0.59	0.82
Sulfate	0.94	0.85	0.92	0.98

693

694   Figure 6.